Article:
Hobbs, M. orcid.org/0000-0003-4661-692X, Zhu, C., Grainger, M. et al. (2 more authors) (2018) Quantitative traceable temperature measurement using novel thermal imaging camera. Optics Express, 26 (19). 24904-24916. ISSN 1094-4087

https://doi.org/10.1364/OE.26.024904

Research Article | Vol. 26, No. 19 | 17 Sep 2018 | OPTICS EXPRESS 24904
Optics EXPRESS

Quantitative traceable temperature measurement using novel thermal imaging camera

MATTHEW J. HOBBS, CHENGXI ZHU, MATTHEW P. GRAINGER, CHEE HING TAN, AND JON R. WILLMOTT*

Department of Electronic and Electrical Engineering, The University of Sheffield, Sheffield, S1 4DE, UK
**j.r.willmott@sheffield.ac.uk*

Abstract: Conventional thermal imaging cameras, based on focal-plane array (FPA) sensors, exhibit inherent problems: such as stray radiation, cross-talk and the calibration uncertainty of ensuring each pixel behaves as if it were an identical temperature sensor. Radiation thermometers can largely overcome these issues, comprising of only a single detector element that can be optimised and calibrated. Although the latter approach can provide excellent accuracy for single-point temperature measurement, it does not provide a temperature image of the target object. In this work, we present a micromechanical systems (MEMS) mirror and silicon (Si) avalanche photodiode (APD) based single-pixel camera, capable of producing quantitative thermal images at an operating wavelength of 1 µm. This work utilises a custom designed f-theta wide-angle lens and MEMS mirror, to scan +/– 30° in both x- and y-dimensions, without signal loss due to vignetting at any point in the field of view (FOV). Our single-pixel camera is shown to perform well, with 3 °C size-of-source effect (SSE) related temperature error and can measure below 700 °C whilst achieving ± 0.5 °C noise related measurement uncertainty. Our measurements were calibrated and traceable to the International Temperature Scale of 1990 (ITS-90). The combination of low SSE and absence of vignetting enables quantitative temperature measurements over a spatial field with measurement uncertainty at levels lower than would be possible with FPA based thermal imaging cameras.

References and links

1. M. Vollmer and K.-P. Möllmann, *Infrared Thermal Imaging: Fundamentals, Research and Applications* (John Wiley & Sons, 2017).
2. Q. He, Z. Su, Z. Xie, Z. Zhong, and Q. Yao, "A novel principle for molten steel level measurement in tundish by using temperature gradient," IEEE Trans. Instrum. Meas. **66**(7), 1809–1819 (2017).
3. R. Usamentiaga, J. Molleda, D. F. Garcia, J. C. Granda, and J. L. Rendueles, "Temperature measurement of molten pig iron with slag characterization and detection using infrared computer vision," IEEE Trans. Instrum. Meas. **61**(5), 1149–1159 (2012).
4. S. K. Everton, M. Hirsch, P. Stravroulakis, R. K. Leach, and A. T. Clare, "Review of in-situ process monitoring and in-situ metrology for metal additive manufacturing," Mater. Des. **95**, 431–445 (2016).
5. J. Dixon, "Radiation thermometry," J. Phys. E Sci. Instrum. **21**(5), 425–436 (1988).
6. P. Saunders, *Radiation Thermometry: Fundamentals and Applications in the Petrochemical Industry* (SPIE, 2007).
7. H. W. Yoon and G. P. Eppeldauer, "Measurement of thermal radiation using regular glass optics and short-wave infrared detectors," Opt. Express **16**(2), 937–949 (2008).
8. N. Boone, C. Zhu, C. Smith, I. Todd, and J. R. Willmott, "Thermal near infrared monitoring system for electron beam melting with emissivity tracking," Addit. Manuf. **22**, 601–605 (2018).
9. J. Envall, S. Mekhontsev, Y. Zong, and L. Hanssen, "Spatial scatter effects in the calibration of IR pyrometers and imagers," Int. J. Thermophys. **30**(1), 167–178 (2009).
10. G. Grgić and I. Pušnik, "Analysis of thermal imagers," Int. J. Thermophys. **32**(1–2), 237–247 (2011).

#332143 https://doi.org/10.1364/OE.26.024904
Journal © 2018 Received 15 Jun 2018; revised 16 Aug 2018; accepted 17 Aug 2018; published 10 Sep 2018

Optics EXPRESS

11. H. Budzier and G. Gerlach, "Calibration of uncooled thermal infrared cameras," J. Sens. Sens. Syst. **4**(1), 187–197 (2015).
12. A. Whittam, R. Simpson, and H. McEvoy, "Performance tests of thermal imaging systems to assess their suitability for quantitative temperature measurements," in *12th International Conference on Quantitative InfraRed Thermography* (QIRT, 2014).
13. R. Siegel and J. R. Howell, *Thermal radiation heat transfer* (Hemisphere Publishing Corporation, 1992).
14. A. Tapetado, J. Díaz-Álvarez, M. H. Miguélez, and C. Vázquez, "Two-color pyrometer for process temperature measurement during machining," J. Lightwave Technol. **34**(4), 1380–1386 (2016).
15. D. Ng and G. Fralick, "Use of a multiwavelength pyrometer in several elevated temperature aerospace applications," Rev. Sci. Instrum. **72**(2), 1522–1530 (2001).
16. T. Duvaut, "Comparison between multiwavelength infrared and visible pyrometry: application to metals," Infrared Phys. Technol. **51**(4), 292–299 (2008).
17. S. Deemyad, A. N. Papathanassiou, and I. F. Silvera, "Strategy and enhanced temperature determination in a laser heated diamond anvil cell," J. Appl. Phys. **105**(9), 093543 (2009).
18. A. S. Machikhin, P. V. Zinin, A. V. Shurygin, and D. D. Khokhlov, "Imaging system based on a tandem acousto-optical tunable filter for in situ measurements of the high temperature distribution," Opt. Lett. **41**(5), 901–904 (2016).
19. M. J. Hobbs, M. P. Grainger, C. Zhu, C. H. Tan, and J. R. Willmott, "Quantitative thermal imaging using single-pixel Si APD and MEMS mirror," Opt. Express **26**(3), 3188–3198 (2018).
20. V. Milanović, A. Kasturi, J. Yang, and F. Hu, "Closed-loop control of gimbal-less MEMS mirrors for increased bandwidth in LiDAR applications," Proc. SPIE **10191**, 101910N (2017).
21. R. Usamentiaga, D. F. Garcia, and J. Molleda, "Uncertainty analysis in spatial thermal measurements using infrared line scanners," IEEE Trans. Instrum. Meas. **57**(9), 2074–2082 (2008).
22. M. F. Duarte, M. A. Davenport, D. Takbar, J. N. Laska, T. Sun, K. F. Kelly, and R. G. Baraniuk, "Single-pixel imaging via compressive sampling," IEEE Signal Process. Mag. **25**(2), 83–91 (2008).
23. M.-J. Sun, M. P. Edgar, D. B. Phillips, G. M. Gibson, and M. J. Padgett, "Improving the signal-to-noise ratio of single-pixel imaging using digital microscanning," Opt. Express **24**(10), 10476–10485 (2016).
24. Land Instrument International, "LSP-HD - infrared linescanners," https://www.ametek-land.com/-/media/ametekландinstruments/documentation/products/fixedthermalimagerslinescanners/lsphd/ametek_land_lsp-hd_brochure_0310_en.pdf.
25. M. P. Edgar, G. M. Gibson, R. W. Bowman, B. Sun, N. Radwell, K. J. Mitchell, S. S. Welsh, and M. J. Padgett, "Simultaneous real-time visible and infrared video with single-pixel detectors," Sci. Rep. **5**(1), 10669 (2015).
26. H. Preston-Thomas, "The international temperature scale of 1990 (ITS-90)," Metrologia **27**(1), 3–10 (1990).
27. Land Instruments International, "SPOT - high precision pyrometers," https://www.ametek-land.com/-/media/ametekландinstruments/documentation/products/fixedspotnoncontactthermometers/spot/ametek_land_spot_brochure_marcom0355_rev_15.pdf.
28. R. Gade and T. B. Moeslund, "Thermal cameras and applications: a survey," Mach. Vis. Appl. **25**(1), 245–262 (2014).
29. Hamamatsu Photonics, "Si APD - S12426 series," *https://www.hamamatsu.com/resources/pdf/ssd/s12426_series_kapd1047e.pdf*.
30. Land Instruments International, "Cyclops L - a family of high precision portable non-contact pyrometers," https://www.ametek-land.com/-/media/ametekландinstruments/documentation/products/portablenoncontactthermometers/cyclops/ametek_land_cyclops_brochure_rev6_en.pdf.
31. T. Williams, *Thermal imaging cameras: characteristics and performance* (CRC, 2009).
32. J. Bezemer, "Spectral sensitivity corrections for optical standard pyrometers," Metrologia **10**(2), 47–52 (1974).
33. P. Saunders, "Uncertainty arising from the use of the mean effective wavelength in realizing ITS-90," in *AIP Conference Proceedings* (AIP, 2003), pp. 639–644.
34. Land Instruments International, "SPOT - user guide," https://www.ametek-land.com/-/media/ametekландinstruments/documentation/products/fixedspotnoncontactthermometers/spot/ametek_land_808273_spot_pyrometer_user_guide_issue_11.pdf.

1. Introduction

Thermal imaging cameras are commonly used in manufacturing and industrial processing for fault detection, temperature measurement and process control [1–4]. Qualitative thermal imaging enables the detection of hot spots or defects within the process, by identifying and resolving temperature differences across the target object. However, when the measurement of absolute temperature is required, a quantitative approach to thermal imaging should be used. Such applications require the measurement of temperature not simply at a single-point upon the target, which could be provided by the use of a single-pixel radiation thermometer [5–7], but over a spatial field, in the form of a thermal image temperature map.

Optics EXPRESS

Photon detector based focal-plane array (FPA) thermal imaging cameras are the fastest thermal imaging technology available for standard imaging formats. Typical near infrared silicon (Si) based FPA cameras, for process imaging, may offer frame rates of > 60 Hz for resolutions of 2048 by 2048 pixels, with diminishing frame rates and resolution at longer wavelengths [8]. Lower temperatures must be imaged at longer wavelengths, with generally more expensive technology; these are often designed around inherently expensive thermoelectrically or cryogenically cooled photon detectors. Lower cost thermal detector based instruments are an alternative, however, the low cost is at the expense of lower sensitivity and longer response time. The use of FPA based thermal imaging cameras for accurate quantitative temperature measurements provides significantly increased measurement uncertainties compared to radiation thermometers. Measuring temperature with these cameras provides additional challenges which are inherent to their FPA. Such problems include inter-pixel cross-talk and stray radiation, with the size-of-source effect (SSE) being a major contributor to the latter [9,10]. It is very challenging to devise a calibration scheme that can ensure each pixel behaves as if it were an identical radiation thermometer [11]. The various inherent properties of FPA based thermal imaging cameras leads to errors when trying to use them for accurate quantitative temperature measurements [12].

Another consideration for the realisation of an accurate temperature measurement is the emissivity of the target object. Emissivity is the ratio of radiated emittance from a target to that of a perfect blackbody, at the same temperature, wavelength and viewing angle. It is highly dependent upon the surface conditions of the material [13]. Its value may be a priori known and, therefore, factored into the temperature calculation within the instrument processing algorithms. However, if emissivity is not known, one approach would be to perform the measurement over different spectral ranges using a ratio radiation thermometer [14] or a wavelength scanning technique [15–17]. Ratio radiation thermometers perform the measurement using two closely spaced wavelength bands (channels) where it is assumed that the emissivity is the same for each channel; the measured temperature is, therefore, related to the ratio between the two channels. Wavelength scanning techniques involve taking measurements at multiple narrow wavelength bands, by, for example, utilising a variable optical filter. Such an approach provides more spectral emissivity information to the temperature calculation, at the expense of limiting the minimum measureable temperature. Increasing the number of wavelength points exacerbates this issue or dictates the need for longer acquisition time. The detector could be exchanged for a FPA, to enable spectral imaging over a spatial field [18], although the aforementioned issue of SSE is still deleterious for quantitative temperature measurement uncertainty.

We previously presented work on the development of a single-pixel scanning thermal imaging system that demonstrated some features required to enable quantitative thermal imaging [19]. The system featured a micromechanical systems (MEMS) mirror, positioned upon two-axis actuators utilising a beam steering technique [20] to scan the field of view (FOV) of a single-pixel over the target. This was in contrast to other single-pixel imaging techniques, such as rotating mirrors [21] and digital micromirror devices (DMDs) [22,23]. Rotating mirror cameras are ideal for scanning lines of temperature at line rates up to 150 Hz for measurement of 1000 points [24]. These systems offer reduced SSE, simplified calibration and are suitable for integrating a wide range of photodetectors for various temperature ranges. DMDs enable a more cost effective method of imaging in the near and short-wave infrared, compared to FPAs, whilst the utilisation of compressive sampling algorithms enables reduction in the acquisition time. There is a natural trade-off between frame rate and resolution; for instance, Edgar et al. demonstrate frame rates of ~10 and ~2.5 Hz for resolutions of 32 by 32 and 64 by 64, respectively [25]. However, to the best of our knowledge, DMDs have not yet been demonstrated for quantitative temperature measurements.

Optics EXPRESS

In our new work presented here, we have, for the first time, developed a practical 1 µm MEMS based single-pixel thermal imaging camera and tested it for quantitative temperature measurements against the International Temperature Scale of 1990 (ITS-90) [26]. This provided us with a camera having traceable measurement uncertainty to the SI, demonstrating quantitative temperature mapping of scenes 64 mm by 48 mm, at a focus distance of 300 mm. We developed a custom designed f-theta lens that enabled wide target area scanning without vignetting related measurement error; with an angular FOV of +/– 30°, in both the x- and y-dimensions. Compared to our previous work, a larger area MEMS mirror was integrated into the system, leading to reduced f-number and resulting in improved SNR. We also reduced the pixel integration time to 400 µs, which increased the data capture rate and produced thermal images in a standard format of 160 by 120 pixels, in under 8 seconds. Our new single-pixel camera is capable of measuring below 700 °C whilst achieving a measurement uncertainty, related to electronic noise, of better than ± 0.5 °C. This is an important typical maximum noise parameter for radiation thermometry [27].

2. Camera design and experimental procedures

The single-pixel camera setup used for single-pixel thermal imaging is shown in Fig. 1.

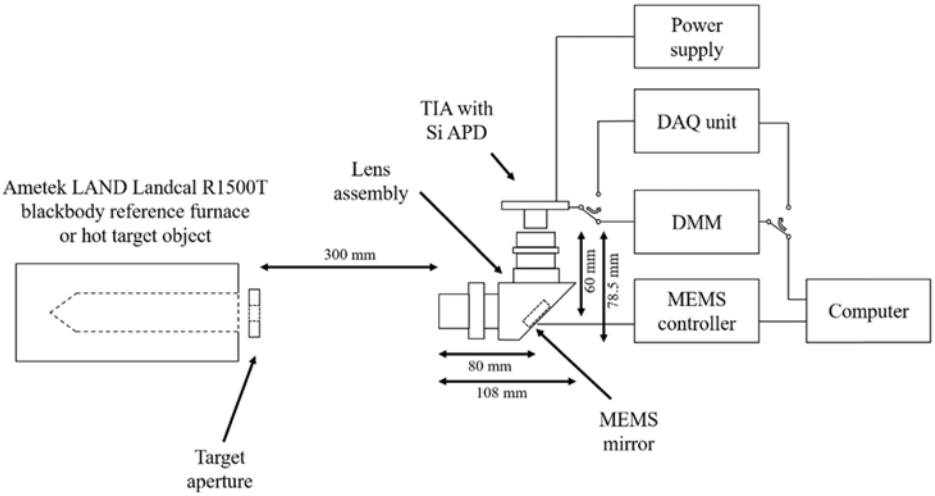

Fig. 1. Single-pixel camera thermal imaging setup. DAQ unit replaces DMM for noise measurement; furnace can alternatively be replaced by a hot object.

The resolution of our thermal images is not limited to fixed dimensions because the MEMS mirror positions can be defined in software. In this work, an array of 160 by 120 measurements was chosen because it is a standard thermal imaging format [28]. The corresponding MEMS mirror positions were pre-loaded into the locally stored flash memory of a Mirrorcle Technologies MEMS controller. The single-pixel's FOV was scanned over the horizontal and vertical positions across the target using a bi-directional raster scanning pattern. The APD active area was 0.2 mm; a small active area is required to minimise the FOV of the single-pixel. This improves measurement resolution, whilst also limiting detector noise caused by dark current and capacitance. In order to reduce reflections that were due to the APD die metal contacts, a 0.8 mm diameter aperture glare stop was placed directly above the detector package. An RG850 filter was positioned in front of the glare stop, to reduce the ambient light reaching the detector and to reduce the dynamic range required of the acquisition electronics. The total spectral band of the instrument was, therefore, between 0.85 and 1.1 µm; with the cut-on wavelength limited by the RG850 filter and the cut-off wavelength limited by the long wavelength sensitivity edge of the APD. The APD's peak

Optics EXPRESS

response wavelength was quoted by the manufacturer as 0.84 µm. The measured signal was converted to a photocurrent by the APD and amplified and converted to a voltage by a transimpedance amplifier (TIA). This voltage was logged by a MATLAB controlled Keysight Technologies 34465A digital multimeter (DMM) set to an integration time of 400 µs. The Hamamatsu S12426-02 low bias voltage Si APD [29] was used with a conventional TIA comprising a Texas Instruments OPA657 op-amp and a resistor-capacitor (RC) feedback network of 2 MΩ and 1.8 pF, respectively. This was followed by a first order RC filter (1 kΩ and 1 nF) for additional noise filtering. Therefore, the overall circuit response time was approximately 10 µs; this was significantly faster than the integration time of the DMM, which is currently the temporal bottleneck within our acquisition system. To provide a constant high voltage to the APD, a Laser Components ABC550-06 high voltage biasing module was used; the optimum bias voltage for peak SNR ratio was found to be at approximately −105 V. The APD was highly sensitive to variations in ambient temperature; the temperature coefficient of its breakdown voltage was 1.1 V/°C, which would lead to a slight variation in gain drift as a function of ambient temperature. Therefore, ambient temperature correction was applied to the biasing module using measurements from a 2 kΩ temperature sensor that was placed near to the APD. This enabled adjustments to the bias voltage and ensured the APD gain was stabilised.

The implementation of a practical-to-use single-pixel camera required the design of an f-theta optical system. Our lens consisted of five elements and two groups. A comparatively large Mirrorcle Technologies MEMS mirror, 5 mm in diameter, was set in between the two lens groups. The design focal length of the lens was 18 mm. For every 100 mm further from the camera, the measurement area for each mirror location was, therefore, designed to increase by 1 mm; the design FOV was 100:1 in radiation thermometer nomenclature. Calculation of temperature from the measured output voltage, for each pixel, can be achieved using the Wien approximation to Planck's law [19]. Calibration took place with our camera sighted on a 10 mm aperture that was placed directly in front of the furnace aperture. To ensure our measurements were traceable to ITS-90, the furnace temperature was measured using a UKAS certified Ametek LAND Cyclops 100L reference thermometer [30] prior to each measurement. This thermometer was quoted by the manufacturer to measure with accuracy of 0.25%K and repeatability of 0.1%K of the reading, with an operational wavelength of 1 µm. This reference thermometer (transfer standard) was traceable to an original reference thermometer, at the UK National Measurement Institute, which was calibrated against high temperature fixed points, according to the definitions and procedures within ITS-90 [26].

A key parameter that is used for measuring the quality of camera images is the modulation transfer function (MTF). MTF is a measure of the spatial frequencies that a camera can resolve and quantifies its ability to distinguish contrast within an image [1,31]. A simple method we used for assessment of the single-pixel camera MTF was based on the 1951 USAF test pattern. This consisted of a metal plate featuring equally spaced bar targets alternating between open and opaque sections, ranging from slit widths of 7 mm, to 0.5 mm, as shown in Fig. 2. The single-pixel camera imaged each bar target, with the cross section of each image taken and normalised relative to the maximum and minimum of the 7 mm measurement. The maximum, I_{max}, and minimum, I_{min}, of each of these image cross-sections were taken and used to calculate the system level MTF. This included both the APD and electronic system of the camera, using (1), which is plotted as a function of the spatial frequency, the inverse of the slit width.

Optics EXPRESS

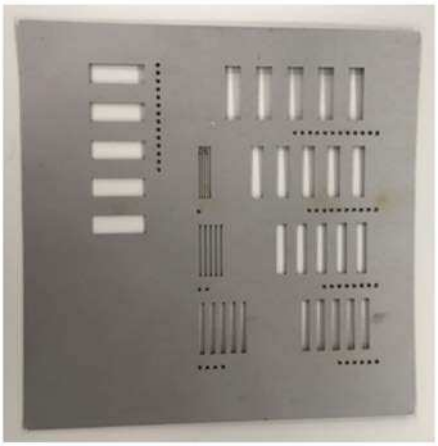

Fig. 2. MTF test plate used for spatial frequency assessment.

$$MTF = \frac{I_{\max} - I_{\min}}{I_{\max} + I_{\min}} \quad (1)$$

The imaging resolution can be defined as the spatial frequency corresponding to an MTF of 0.5, such that image areas with spatial frequencies lower than this value are taken to be resolved sufficiently well for qualitative imaging purposes. For quantitative temperature measurements, we define the measurement FOV as containing 90% of the radiant power emitted by a target source that is twice the diameter of the paraxial image of the APD's optically responsive area. We, therefore, considered sections of the image with longer spatial frequency variations than this value to contain accurate radiometric measurements. Both of these criteria accord with standard practices in thermal imaging and radiation thermometry, respectively [9,27].

D* related temperature noise [31] was measured by setting the single-pixel camera to its 0°, 0° origin position. A Labview controlled National Instruments USB-6212 data acquisition (DAQ) unit was used to log data every 10 µs over a 10 s period. This enabled the data to be integrated at different time periods, to assess the effect that varying the data acquisition time would have on the camera noise performance. The root-mean-squared (RMS) noise was calculated by dividing the noise as a percentage of the measurement (100 × standard deviation / mean) by the percentage change in measured radiance for a one degree Celsius change in target temperature (%/°C) of the measurement for each target temperature. The %/°C value depends upon the mean effective wavelength of the measurement; which is the average wavelength of the spectral response of the detector over the measured temperature range [32,33]. Noise manifests as a fluctuation in the measured temperature, which we measured within ± 1 standard deviation of the mean.

Silhouettes of various target objects were acquired by placing them in front of a furnace that was heated to 1000 °C; measuring 993 °C using our reference thermometer. The single-pixel camera was also focused on a hot target object, to demonstrate its thermal imaging capabilities in a representative use-case.

3. Results and discussion

A suite of measurements were performed on our single-pixel camera following calibration, with the main aim of elucidating the performance of spatial and thermal resolution. A 3D printed titanium lattice was imaged by the single-pixel camera; firstly, illuminated with near infrared radiation from a halogen light source and secondly with it heated to a high temperature using a butane propane torch flame. Figure 3 shows (a) a photograph of the target, (b) an image of the target with near infrared illumination, (c) an uncalibrated raw data

Optics EXPRESS

radiance image of the heated lattice and (d) a calibrated temperature map of the heated lattice. Both the illuminated image and the uncalibrated radiance image indicate that the single-pixel camera can resolve relatively fine features within the lattice. The calibrated image indicates that the temperature at the point where the flame impinged the lattice rose to over 1100 °C. The measured temperature then decreased in all three dimensions moving away from this point, indicating the reduction in the temperature of the lattice. With the camera focused at 300 mm from the furnace, the overall imaging scan area was 64 mm by 48 mm with a total image capture time of under 8 seconds.

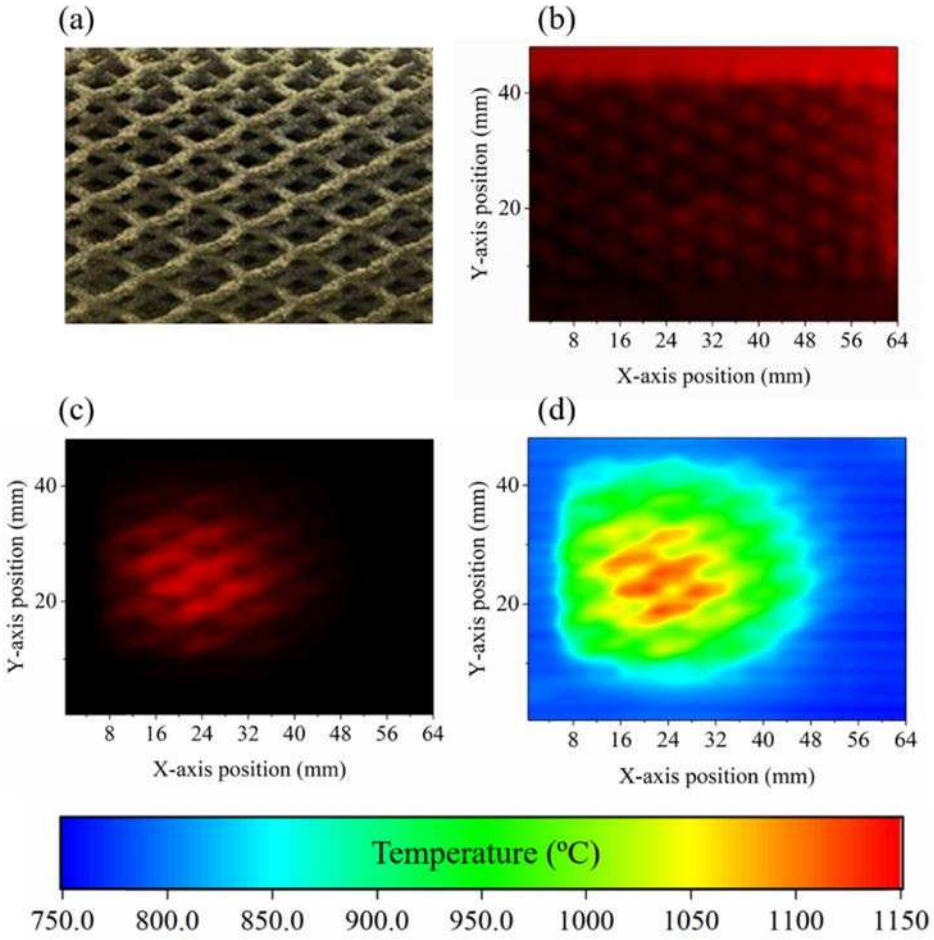

Fig. 3. Target object imaging of 3D printed titanium lattice: (a) visible image of target, (b) near infrared illuminated target image, (c) uncalibrated raw data image of heated target and (d) calibrated temperature map of the heated target. The emissivity of the titanium lattice is a priori assumed to be 0.55 [34].

The surface emissivity of the titanium lattice is a priori assumed to be 0.55 [34], which is factored into the calibration of the image in Fig. 3(d). If emissivity were to be ignored, or synonymously assumed to have a value of 1.0, when performing the temperature measurement, the resulting measurement would read “low”. Subsequent measurements in this work were performed using a calibrated approximate blackbody reference furnace, with a specified emissivity of 0.998. Therefore, any emissivity related error was assumed to be negligible. Additionally, the reference thermometer was sensitive to the same band of

Optics EXPRESS

wavelengths as our instrument, therefore, the residual emissivity uncertainties approximately cancelled.

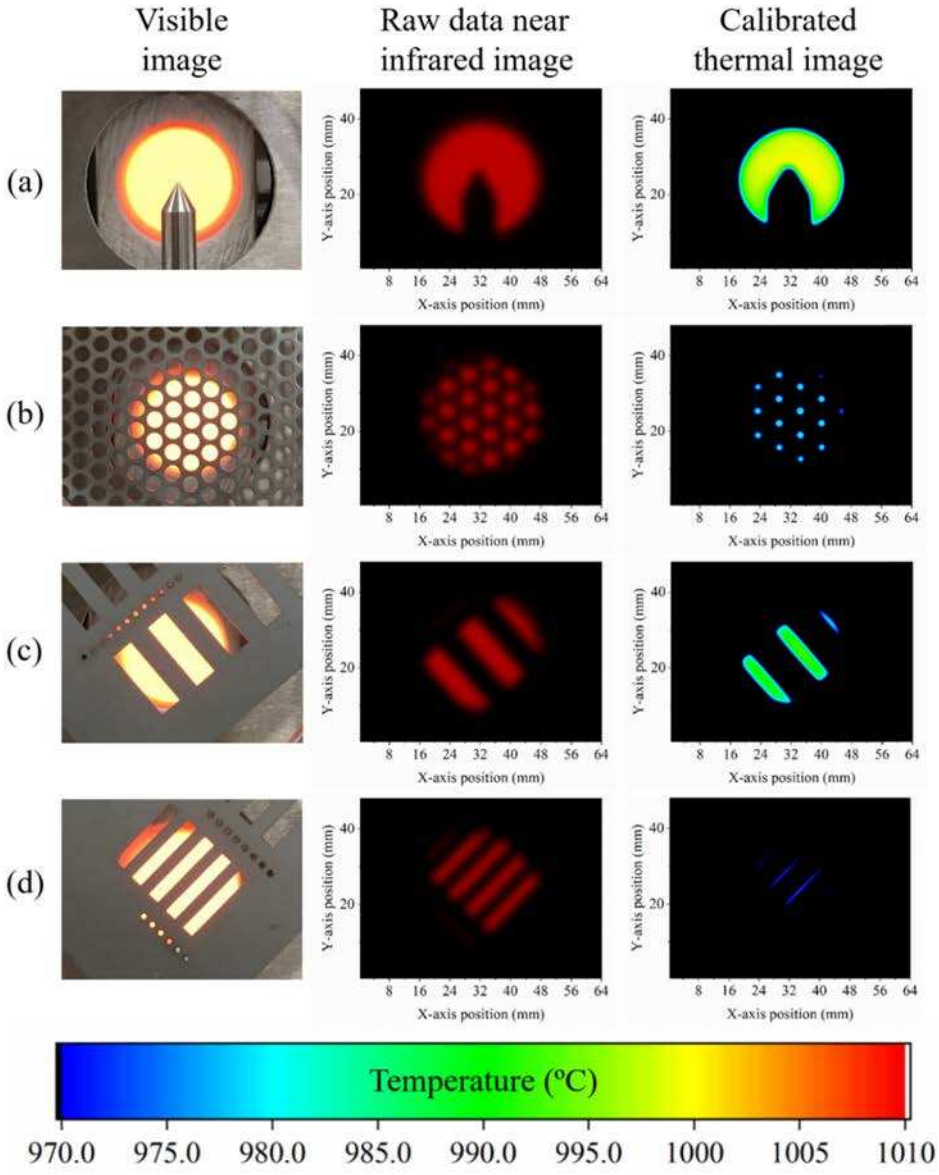

Fig. 4. Target object imaging of (a) a narrowing point, (b) a mesh with 5 mm holes, (c) 6 mm wide slits and (d) 3 mm wide slits. Each object is shown with a visible image, a raw data near infrared image and a calibrated temperature map image. Furnace temperature was 993 °C.

Radiometrically accurate measurements were made with reference to an approximate blackbody using the furnace and target objects, assuming a near ideal emissivity measurement scenario. The aim was to demonstrate quantitative imaging and the single-pixel camera's ability to measure with traceability to ITS-90. Figure 4 shows images of (a) a narrowing point, (b) a mesh with 5 mm holes, (c) 6 mm wide slits and (d) 3 mm wide slits. For each target object, we show a photograph of the target, an uncalibrated raw data near infrared

Optics EXPRESS

radiance image and a quantitative calibrated temperature map. The calibrated temperature map range was limited to between 970 and 1010 °C to demonstrate how the temperature measurement compared to the 993 °C that was indicated by our reference thermometer.

The signal intensity images superficially correspond well with the visible images; there is good distinction of features, which are replicated in the signal intensity images. Some blurring can be seen when the pixel FOV moves between the opaque target and the open furnace aperture; the signal from each pixel measures an average of the area the FOV moves across. This highlights the need to minimise the FOV of the single-pixel camera, leading to increased spatial frequency and the ability to resolve finer details. The system level MTF of the single-pixel camera was measured and plotted as a function of spatial frequency in Fig. 5. With a specified MTF of 0.5, a spatial frequency of 0.6 mm^{-1} was measured, which corresponds to a qualitative measurement resolving of feature sizes below 1.67 mm.

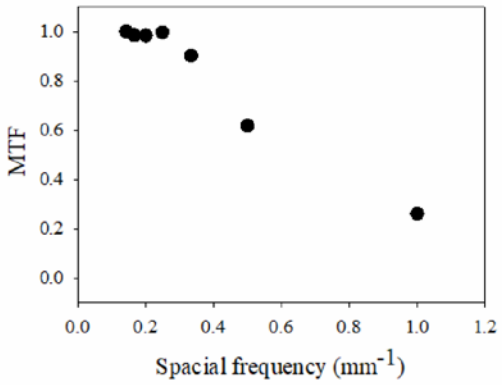

Fig. 5. Single-pixel camera MTF as a function of spatial frequency. Furnace temperature of 993 °C.

As described above, the single-pixel camera appears ideal for qualitative imaging applications, such as the detection of hot spots upon targets. We investigate the quantitative measurement performance below.

Temperatures corresponding only to 970 °C and above are shown in Fig. 4, for the calibrated images. From a quantitative point of view, for the determination of an accurate temperature measurement, the finer details within the image measure below their thermodynamic temperature, which results in a temperature measurement error. This is equivalent to the error due to under filling the FOV of a conventional radiation thermometer. Recapitulating: if the FOV is large compared to the size of the feature or object being measured, radiation thermometry will not provide an accurate temperature measurement and a measurement will be made which is below the true surface temperature, resulting in the thermometer measuring “low”. Our single-pixel camera also measures low when the pixel FOV moves between the exposed parts of the furnace and those covered by the silhouette. The corollary is that, as the exposed furnace area is increased, and the instrument gathers radiation from a larger area, there is a SSE contribution to the temperature measurement resulting in a measurement which is greater than the true surface temperature.

To further assess our single-pixel camera’s quantitative measurement capabilities, fully calibrated thermal images are shown in Fig. 6 for a furnace temperature of 993 °C with varying diameter target apertures from 5 to 25 mm. There is some non-uniformity in the measured temperature across each of the apertures, and a reduction in the measured temperature at the periphery of each aperture. Increase in target aperture diameter results in a concomitant increase in the measured temperature. If we measure a centre-line across our

Optics EXPRESS

images of the apertures, using the uncalibrated raw data, the full width at half maximum (FWHM) yields an accurate measure of the true aperture diameter.

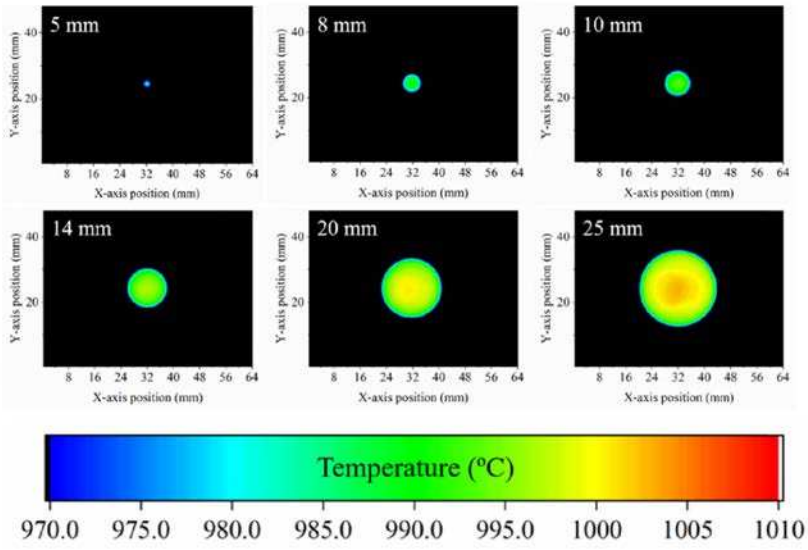

Fig. 6. Target aperture imaging shown for target apertures of 5, 8, 10, 14, 20 and 25 mm in diameter. Furnace temperature of 993 °C.

Cross-sections of each image were taken across the aperture mid-points and are shown in Fig. 7. They clearly show the image non-uniformity, the increase in measured temperature with increasing target aperture diameter and the reduction in measured temperature at the aperture periphery. There is approximately 9 °C increase in measured temperature, comparing the peak readings of the 10 and 25 mm aperture measurements as a result of SSE, which can result from a variety of factors. Within our single-pixel camera, SSE is likely to be due to stray reflections from the imperfectly blackened metalwork and some scattering from optical elements. The FOV and SSE related error are within usual bounds for radiation thermometry and our camera is able to measure the temperature of relatively fine or large features.

Due to the single-pixel nature of the camera, we find in section 4 below that it is possible to reduce the SSE by means of simple optical baffles and reduce the related temperature error with further instrument optimisation.

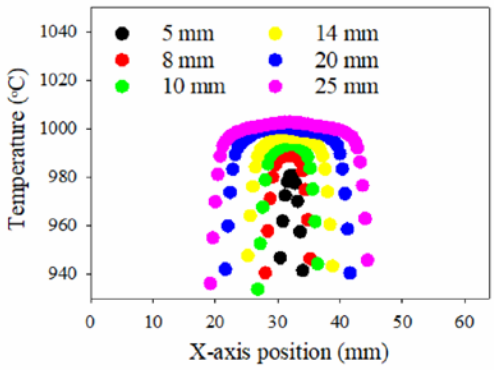

Fig. 7. Mid-point cross sections of aperture images. Furnace temperature of 993 °C.

Optics EXPRESS

Figure 8 shows a FOV and SSE measurement for our single-pixel camera, with varying target aperture diameters, with the furnace measuring a constant temperature of 993 °C. This measurement was repeated at several different scan-angles in both the x- and y-dimensions, up to the angle-repeatability limits of the MEMS mirror. The camera FOV corresponding to 90% energy was found at a FOV of approximately 60:1, which is larger than suggested by theoretical modelling of the optics system. SSE leads to the measured temperature reading high, as expected from analysis of Fig. 7.

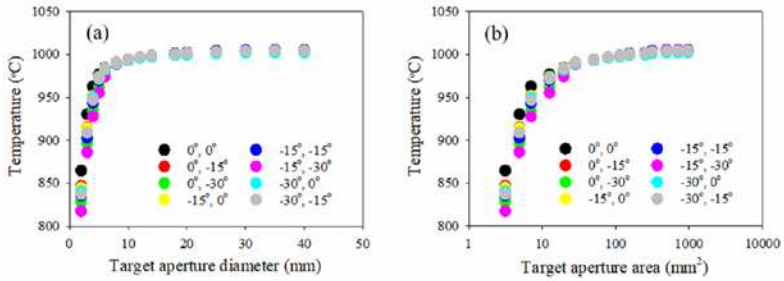

Fig. 8. FOV and SSE results at different single-pixel camera scan angles ranging from its 0°, 0° origin position and its maximum scan angle for a 993 °C furnace. Measured temperature shown as function of (a) target aperture diameter and (b) target aperture area.

A critical feature in the design of the f-theta lens system was that it should be able to scan over as large a target area as possible without vignetting. For this criterion to be achieved, there must be no reduction in signal due to the angle of the MEMS mirror within the optical system, when imaging an optically uniform target. Such a reduction would lead to a temperature measurement error. As can be seen in Fig. 8 for the FOV and SSE measurements at various camera scan angles, once electronic noise is accounted for, there is no significant change in the measured temperature when the camera's optics are tested at its various field positions. Table 1 shows the measured temperature for the 10 mm target aperture, using the single-pixel camera in comparison with the calibration reference thermometer at the camera's various pixel locations within the scene. We estimated the repeatability of our single-pixel camera to be similar to that quoted for the reference thermometer and calculated the uncertainties using quadrature addition. The result was a calculated measurement uncertainty for the reference thermometer of ± 1.7 °C and a measurement uncertainty for our single-pixel camera of ± 1.8 °C. This result confirms the ability of the camera to accurately measure the target temperature over a wide scene. With the full camera field utilised, it is able to image a target area of 350 mm in diameter using our current configuration with angular FOV of ± 30° in both the x- and y-dimensions.

Table 1. Temperature measured by single-pixel camera at different scan angles for 10 mm target aperture in comparison with reference thermometer. Uncertainty with respect to the SI was calculated to be ± 1.7 °C for reference thermometer and estimated to be ± 1.8 °C for single-pixel camera.

	Temperature measurement (°C)	
Scan angle (°)	MEMS camera	ITS-90 reference thermometer
0, 0 (origin)	994.2	993
0, –15	994.2	993
0, –30	993.7	993
–15, –0	993.7	993
–15, –15	994.1	993
–15, –30	993.3	993
–30, 0	993.7	993
–30, –15	994.7	993

Optics EXPRESS

The noise performance was analysed with the single-pixel camera set to its 0°, 0° origin position, with results shown in Fig. 9. The acquisition of measurements for this test took place over a 10 second period, with a 400 µs integration time, which was consistent with the single-pixel imaging measurements above. Integration times of 10 µs and 4 ms are also included in Fig. 9 for comparison.

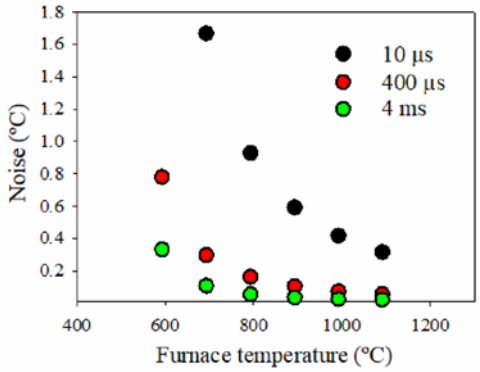

Fig. 9. Single-pixel camera noise with target temperature at different integration levels.

A design specification of ± 0.5 °C between target temperatures of 600 and 700 °C is typical for a 1 µm commercial radiation thermometer. It was found that a ± 0.5 °C noise specification for our single-pixel camera could be achieved below a target temperature of 700 °C, with the 400 µs integration time. As indicated above, this is an important performance metric and demonstrates our system works well as a radiation thermometer, in addition to producing thermal images. If the integration time were increased to 4 ms, this noise specification could be achieved below 600 °C, though this would be at the expense of a longer image capture time. Alternatively, integration time can be reduced to enable faster data capture. For the image resolution demonstrated in this work, an integration time of 10 µs would lead to a total image capture time of approximately 164 ms, equating to a frame rate of over 6 Hz. By way of illustration, for an integration time of 10 µs, the ± 0.5 °C noise is measured to be approximately 950 °C; 700 °C could be recorded at this high frame rate, with ± 2 °C of electronic noise.

4. SSE instrument optimisation

The design of our single-pixel camera allowed a straightforward optimisation of the system for stray radiation. In order to reduce the instrument SSE, a 0.8 mm diameter glare stop was originally positioned directly above the detector, resulting in a SSE contribution to our measurement of 9 °C. We replaced this aperture with a 0.6 mm diameter glare stop to attempt to further reduce glare and reflections. This was the minimum diameter that optical raytracing suggested we could use without impinging upon the direct cone of light between aperture stop and detector. Such optimisation is impracticable with a FPA based thermal camera because that would require the placement of a glare stop above each pixel. The MEMS mirror was replaced with another unit, as a second step in the optimisation, whose window was coated with an anti-reflective (AR) coating centred within the wavelength range of the Si APD. FOV and SSE measurements were repeated for the single-pixel camera with the new optimisation at its 0°, 0° origin position, and compared in Fig. 10(a) against the previous, unoptimised, configuration.

Optics EXPRESS

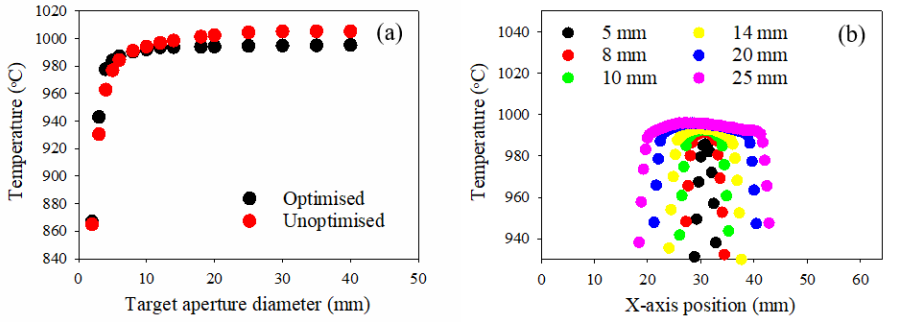

Fig. 10. (a) FOV and SSE results at a 0°, 0° origin position before and after additional optimisation and (b) mid-point cross sections of aperture images after further optimisation. Furnace temperature of 993 °C.

There is a clear reduction in the SSE with the additional optimisation, which leads to a reduction in the SSE related temperature error. With this improved performance, the FOV corresponding to 90% energy is now approximately 75:1, therefore, becoming closer to the design FOV. Imaging of various diameter target apertures was repeated, and their cross sections are shown in Fig. 10(b). If we now directly compare the peak readings of the 10 and 25 mm aperture measurements, the increase in measured temperature has reduced from approximately 9 °C to approximately 3 °C. This is a significant improvement which shows how our single-pixel camera can be optimised in ways which are not possible with FPA cameras. There is scope for further optimisation, potentially by AR coating all lens surfaces, to lower the SSE further, and to render the FOV closer to that of its design.

5. Conclusion

In this work we have demonstrated a unique single-pixel camera for ITS-90 traceable temperature measurements across a thermal image. To our knowledge, this is the first demonstration of a single-pixel camera that can make SI unit traceable temperature measurements of a stationary scene, with a sufficient FOV to produce useful images. Using our wide-angle f-theta lens system, designed specifically for the application, we produced 160 by 120 pixel resolution images with low SSE related temperature error. Operation of the single-pixel camera at its widest scan angles produces images of 350 mm in diameter, at a distance of 300 mm, without introducing temperature measurement error due to vignetting. This combination of low SSE and absence of vignetting enables quantitative spatial temperature measurements with a low level of measurement uncertainty that would not be possible with a FPA based camera. The single-pixel camera accurately measured temperature below 700 °C with better than ± 0.5 °C noise uncertainty in the temperature measurement.

Funding

Engineering and Physical Sciences Research Council (EPSRC) fellowship EP/M009106/1.